



Large-area long-wave infrared broadband all-dielectric metasurface absorber based on markless laser direct writing lithography

CHENG CHEN,¹ YANHUA LIU,^{1,5} ZHOU-YING JIANG,¹ CHONG SHEN,²
YE ZHANG,³ FAN ZHONG,^{3,4} LINSSEN CHEN,¹ SHINING ZHU,³ AND
HUI LIU^{1,6}

¹*School of Optoelectronic Science and Engineering, Key Lab of Advanced Optical Manufacturing Technologies of Jiangsu Province & Key Lab of Modern Optical Technologies of Education Ministry of China, Soochow University, Suzhou, Jiangsu 215006, China*

²*School of Physics, Southeast University, Nanjing 211189, China*

³*National Laboratory of Solid State Microstructures and School of Physics, Collaborative Innovation Center of Advanced Microstructures, Nanjing University, Nanjing 210093 Jiangsu, China*

⁴*Institute of Functional Nano & Soft Materials (FUNSOM), Jiangsu Key Laboratory for Carbon-Based Functional Materials & Devices, Soochow University, Suzhou, Jiangsu 215123, China*

⁵*yhliu@suda.edu.cn*

⁶*liuhui@nju.edu.cn*

Abstract: Scalable and low-cost manufacturing of broadband absorbers for use in the long-wave infrared region are of enormous importance in various applications, such as infrared thermal imaging, radiative cooling, thermal photovoltaics and infrared sensor. In recent years, a plethora of broadband absorption metasurfaces made of metal nano-resonators with plasmon resonance have been synthesized. Still, their disadvantages in terms of complex structure, production equipment, and fabrication throughput, limit their future commercial applications. Here, we propose and experimentally demonstrate a broadband large-area all-dielectric metasurface absorber comprised of silicon (Si) arrays of square resonators and a silicon nitride (Si₃N₄) film in the long-wave infrared region. The multiple Mie resonance modes generated in a single-size Si resonator are utilized to enhance the absorption of the Si₃N₄ film to achieve broadband absorption. At the same time, the transversal optical (TO) phonon resonance of Si₃N₄ and the Si resonator's magnetic dipole resonance are coupled to achieve a resonator size-insensitive absorption peak. The metasurface absorber prepared by using maskless laser direct writing technology displays an average absorption of 90.36% and a peak absorption of 97.55% in the infrared region of 8 to 14 μm, and still maintains an average absorption of 88.27% at an incident angle of 40°. The experimentally prepared 2 cm × 3 cm patterned metasurface absorber by markless laser direct writing lithography (MLDWL) exhibits spatially selective absorption and the thermal imaging of the sample shows that the maximum temperature difference of 17.3 °C can exist at the boundary.

© 2022 Optica Publishing Group under the terms of the [Optica Open Access Publishing Agreement](#)

1. Introduction

Long-wave infrared radiation corresponds to electromagnetic radiation in the wavelength range of 8 to 14 μm, one of the well-known atmospheric windows. Since electromagnetic radiation in this band is able to pass through the earth's atmosphere without being absorbed and scattered, the high-absorption technology related to this band is growing rapidly, and promoting the development of plenty of devices for practical use, including light detection [1,2], radiation cooling [3–5], heat imaging [6–8], infrared sensor [9,10], and thermal photovoltaics [11–13], etc. Due to their excellent absorption performance and spectral tunability, metasurface absorbers continue to attract more and more attention from researchers. Researchers have achieved the

arbitrary management of absorption spectra by controlling the composition of metasurfaces, the resonator geometric shapes, and size of the resonators [14–16]. With the rapid development of related scientific and technological fields, whether military or civilian, long-wave infrared broadband absorbers are required, for further enhancing the performance of microbolometers and night visions [17–20].

Most of the metasurface absorbers utilize the inherent losses in the resonator to produce large absorption. The enhanced local field in the subwavelength resonator with tailored electrical and magnetic resonance increases the absorption and accomplishes near-unity absorption [21]. At present, the widely used metasurface absorbers in metal-insulator-metal (MIM) structures usually result in a narrow-band absorption peak and narrow thermal emission peak due to the limited bandwidth of plasmon resonance [22–27], and it is tough to obtain large absorption in a broadband wavelength range. Generally speaking, to increase the absorption bandwidth of the metasurface absorber, the researchers have mainly proposed two strategies to increase the number of resonance modes so that multiple absorption peaks can appear. The first strategy introduces multiple resonators of different sizes or shapes in a plane super-unit cell, usually composed of 2 to 6 resonators [21,28–31]. The metasurface absorber recombines the adjacent absorption peaks produced by different resonators to achieve a broadband absorption. Due to the limited number of resonators, the bandwidth with absorptivity greater than 90% is about $1 \sim 3 \mu\text{m}$ in the infrared region. For instance, metasurface absorbers composed of four discs and five columns, where each disc and column have different sizes, accomplish an absorption rate of $3.5 \sim 4.1 \mu\text{m}$ and $10 \sim 13 \mu\text{m}$ [32–34]. The second strategy is implemented by stacking multiple layers of MIM [35–37]. To broaden the bandwidth as much as possible, the number of stacked layers can reach up to dozens, which significantly increases the preparation cost and difficulty of manufacturing [38]. A typical implementation of this strategy is a tapered hyperbolic metamaterial absorber, which utilizes the existing slow light waveguide modes to capture and absorb light of different wavelengths at positions of varying tooth widths [39]. Whether it is a super-unit structure or a multi-layer structure, it is challenging to apply these designs even to practical applications, let alone integrate with other platforms. In addition to the above-mentioned infrared broadband metasurface absorber, researchers have recently adopted highly doped semiconductors to obtain broadband absorption, where plasma frequency of semiconductors can be modulated by changing charge carrier concentration [40,41]. The broadband absorption is mainly derived from free carrier absorption and plasmonic resonance supported by the resonator. At the same time, the broadband metal metasurface absorbers mostly utilize the localized surface plasmon resonance of the metal resonator, propagating surface plasmon resonance of the metal thin film, and their combined effect [42]. The nature of the metal material makes the size of the metal resonator much smaller than the sub-wavelength, so that their fabrication process often needs expensive electron beam lithography or focused ion beam lithography and is not compatible with the current complementary metal-oxide-semiconductor (CMOS) process, which is undesirable for its commercial application. Compared with electron beam lithography and focused ion beam lithography technology, MLDWL technology has the advantages of low cost, high efficiency, large preparation area and less environmental disturbance. Therefore, the MLDWL technique provide a new way for the large area all-dielectric metasurface absorber fabrication, which is crucial to the bring the infraed metasurface absorbers into the future practical application. Here, we propose a broadband metasurface absorbers fabricated by MLDWL technology, which is made of Si and Si_3N_4 dielectric materials that has been used in commercial microbolometers.

We propose a novel design methodology to simplify the design and manufacturing process for obtaining a broadband, angle-tolerant long-wave infrared metasurface absorber. It combines a Si resonator with multiple Mie resonance modes with a lossy Si_3N_4 film. It uses the enhanced local field generated by the Si resonator to enhance the absorption by a Si_3N_4 film, thereby making the metasurface absorber have high absorption performance in the entire long-wave infrared spectral

region. The synthesized metasurface absorber has an average absorption higher than 90% and a peak absorption of 97.55% in the infrared region of 8 to 14 μm . At the same time, we utilized the TO phonon resonance in Si_3N_4 to couple with the magnetic dipole resonance in the Si resonator. Resonance coupling causes an abnormal absorption peak, which practically does not produce a significant frequency shift with the change in the size of Si resonator. Even as the incident angle reaches 40° , the metasurface absorber still maintains 88.27% absorption performance, signifying that it is angle-tolerant. In this work, the time required to prepare a $2\text{cm} \times 3\text{cm}$ metasurface absorber by MLDWL is only 25 min. However, it takes 40 hours to prepare samples of the same size using electron beam lithography, and MLDWL is 80 times faster than it. The patterned metasurface absorber displays its spatially selective absorption properties and has the prospect of being integrated into a microbolometer. The process of its preparation is compatible with the CMOS process, which can accelerate its future commercial applications. We believe that the proposed methodology provides new ideas for designing metasurface absorbers in other bands.

2. Experimental section

Numerical Simulations. All the electromagnetic wave simulations were performed using finite-difference-time-domain (FDTD) method in CST Microwave Studio. The simulation adopts unit cell boundaries and Floquet excitation ports. Complex dielectric constants of silicon and silicon nitride are taken from the literature. Thermal simulation is performed using the commercial package Lumerical Device.

Sample Fabrication. A 2 μm thick Si_3N_4 layer and a 2.85 μm thick Si layer grown on a doped Si wafer were obtained by chemical vapor deposition. The prepared wafer sample was spin-coated with AZ1500 photoresist (2500 rpm, 30 s) and baked for 2 min using a hot plate at 90°C . Maskless laser direct writing technology was used to prepare the designed metasurface absorber structures with high efficiency and low cost and the sample was developed with 6% sodium hydroxide solution over 6 s. After that, a 40 nm chromium (Cr) layer was deposited using magnetron sputtering to act as an etching mask. Then acetone was used to lift off photoresist. The silicon resonator was obtained using Reactive Ion Etching (RIE). Lastly, the sample was immersed in a Cr etchant solution to dissolve the Cr etching mask.

Optical Characterization. The reflectance and transmittance measurements of the metasurface absorber was performed by using a Fourier transform infrared spectrometer (Bruker VERTEX 70v). The measured reflectance was normalized to a gold mirror while the measured transmittance was normalized to air. The thermal image is recorded by an infrared camera (FLIR C2). The wavelength range of infrared camera is between 7.5 μm and 14 μm .

3. Results and discussion

By analyzing the previous broadband metasurface absorbers' design concepts, we have concluded that for the metasurface absorber to have high broadband absorption, it is often necessary for the lossy meta-atoms to have multiple resonances at different wavelengths in the spectral region of interest [43]. According to previous studies, by appropriately tuning the size of the high-refractive-index dielectric resonator, it can excite low-order Mie modes in the spectral region of interest and produce local electromagnetic field enhancement near the resonator [44,45]. At the same time, dielectric materials with anomalous properties are naturally accompanied by increased absorption loss in the spectral vicinity of strong absorptive resonances (e.g., TO phonons) [46]. To make the designed dielectric metasurface absorber have broadband high absorption in the infrared atmospheric window (8 ~ 14 μm) and have the advantages like easy optimization and preparation, we propose a strategy of combining single size dielectric resonators with a lossy thin film, utilizing multiple local electromagnetic fields generated by resonator to enhance the absorption by the lossy thin film, and resulting in broadband high absorption. Hence,

we propose a combination of Si resonator array and Si₃N₄ film to achieve broadband absorption in the long-wave infrared window.

To fully understand the origin of the broadband absorption of the proposed all-dielectric metasurface absorber, we explored the reflection and absorption spectra of the Si resonator array, the single-layer Si₃N₄ thin film, and their combination. In the optimized design, the geometric parameters of the square Si resonator array are $h = 2.85 \mu\text{m}$, $w = 3.25 \mu\text{m}$, $p = 6 \mu\text{m}$, and Si₃N₄ film thickness is $2 \mu\text{m}$. Figure 1(a) displays the reflection spectrum and the absorption spectrum of the Si resonator array. We can find that there are multiple perfect reflection peaks caused by the resonance of electric and magnetic dipoles [47–50]. Also, since the imaginary part of the permittivity of Si is almost zero in the long-wave infrared region [51], as shown in Fig. 1(d), there is no absorption in the long-wave infrared region. Figure 1(b) displays the reflectance and absorptivity of the Si₃N₄ film. It has an average absorptivity of 63.5% in the long-wave infrared region, mainly due to the large imaginary part of the permittivity of Si₃N₄. To obtain broadband high absorption, we used the resonance of electric and magnetic dipoles of the Si resonator to enhance the absorption by the Si₃N₄ film. The reflection and absorption spectra of the all-dielectric metasurface absorber are shown in Fig. 1(c). The metasurface absorber designed herein, displays multiple absorption peaks. The perfect absorption peaks at the $9.7 \mu\text{m}$ and $12.6 \mu\text{m}$ are caused respectively by the electric and magnetic dipole resonances of the Si resonator at $9.9 \mu\text{m}$ and $11.8 \mu\text{m}$ enhancing absorption by the Si₃N₄ film. The peak absorptions are 99.6% and 99.4%, respectively. The imaginary part of the permittivity of Si₃N₄ in Fig. 1(d) shows that there is a TO phonon resonance at $12.2 \mu\text{m}$ [52]. It was reported that phonon can be coupled with plasmon modes and it induce enhanced absorption [25]. Here, we observed that the perfect absorption peak of $12.6 \mu\text{m}$ has a larger half-width, which is largely produced by the coupling between the TO phonon resonance of Si₃N₄ at $12.2 \mu\text{m}$ and the magnetic dipole resonance of the Si resonator at $11.8 \mu\text{m}$. During the design process, we did not directly design the Si₃N₄ resonator, mainly because Si₃N₄ has a very large dispersion behavior in the LWIR region, as shown in Fig. 1(d), which hinders the design of broadband absorber structures [53].

To clarify more distinctly that the two perfect absorption peaks are caused by the Mie mode resonance enhancement, Fig. 2(a) illustrates the absolute E-field distributions of the two resonances under the normally incident x-polarized excitation, which proves that the strong local field at $9.7 \mu\text{m}$ mainly appears in the middle of the square resonators, but the strong local field at $12.6 \mu\text{m}$ mainly occurs at the bottom of the square resonators. These local field distributions further point out that the perfect absorption comes from the absorption by the Si₃N₄ film enhanced by the local field. The power loss density distributions in Figs. 7(a, b) also confirm that absorption only exists in the Si₃N₄ film. Although there is a strong local field in the Si resonator, the imaginary part of the permittivity of Si is almost zero. There is no absorption in Si resonators. Figure 2(b) shows the E-field and H-field distributions on the cross-sections of the resonance at $9.7 \mu\text{m}$, where the electromagnetic field distribution corresponds to the electric dipole resonance. Figure 2(c) presents the E-field and H-field distributions on the cross-sections of the resonance at $12.6 \mu\text{m}$, where the electromagnetic field distribution corresponds to the magnetic dipole resonance. At the same time, we believe that impedance matching of the metasurface absorber and the air domain is due to the introduction of the Si₃N₄ film. Also, the incident and the reflected waves produce destructive interference near the interface [54], which reduces the reflection and increases the absorption by the Si₃N₄ film, as shown in **Visualization 1** and **Visualization 2**.

To validate this approach for achieving broadband absorbers in the long-wave infrared region, we utilized MLDWL technology and reactive ion etching (RIE) to efficiently fabricate an all-dielectric metasurface absorber with multiple electric and magnetic dipole resonances. Figure 3(a) shows the schematic diagram of the proposed metasurface absorber, composed of Si resonators array, Si₃N₄ film, and the doped Si substrate. The designed geometric parameters are $h = 2.85$

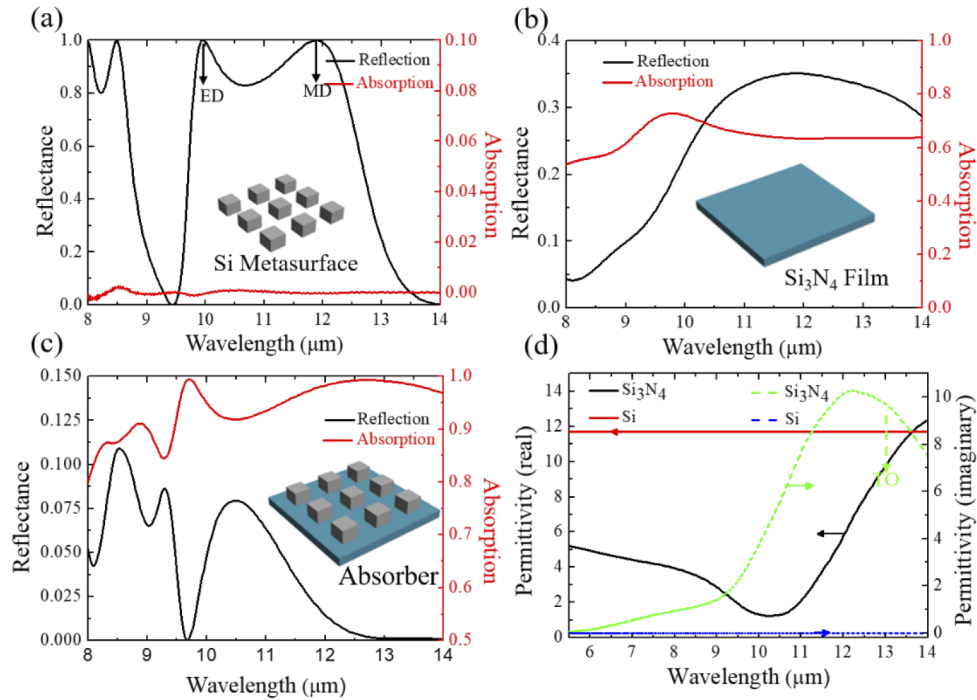


Fig. 1. (a) Reflectance and absorption for an array of Si resonators with $h = 2.85 \mu\text{m}$, $w = 3.25 \mu\text{m}$, a period $p = 6 \mu\text{m}$ (see [Visualization 1](#)). (b) Reflectance and absorption for Si₃N₄ film with $t = 2 \mu\text{m}$. (c) Reflectance and absorption for an array of Si resonators and Si₃N₄ film with the same dimensions as in (a, b) (see [Visualization 2](#)). (d) Real and imaginary permittivities of Si and Si₃N₄ as a function of wavelength.

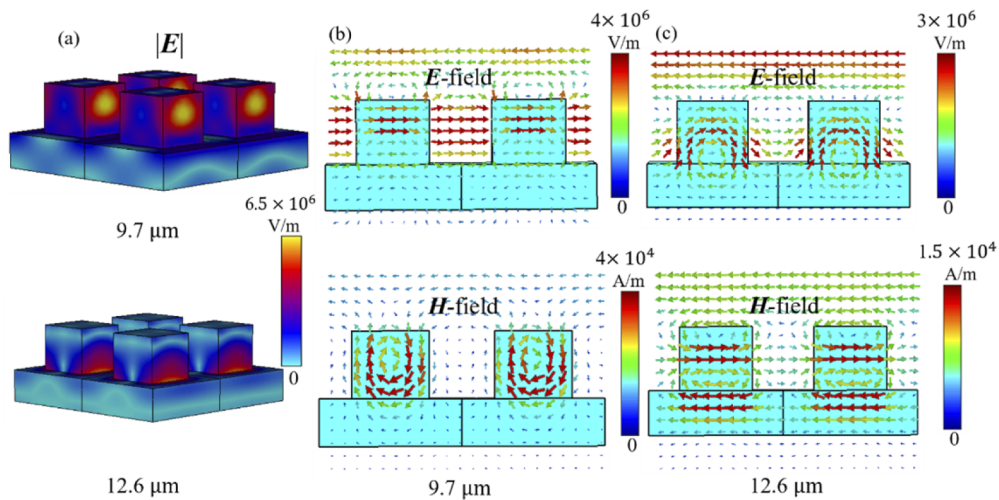


Fig. 2. (a) Simulated absolute E-field distributions at resonance peaks of 9.7 and 12.6 μm, respectively. (b) E-field and H-field on the cross-sections for the resonance at 9.7 μm. The plots show the electric dipole resonance. (c) E-field and H-field on the cross-sections for the resonance at 12.6 μm. The plots show the magnetic dipole resonance.

μm , $w = 3.25 \mu\text{m}$, $p = 6 \mu\text{m}$, and $t = 2 \mu\text{m}$. Figures 3(b, c) are the SEM plane view and three-dimensional view of the as-prepared sample, respectively. As a result of the weak lateral etching characteristics of RIE, the size of the prepared resonators deviates from the design value, and the width of the resonator fabricated in the experiment is about $3.05 \mu\text{m}$. For comparison, we measured the absorption spectra of the all-dielectric metasurface absorber and simulated the absorption spectra with the resonator's width ($w = 3.05 \mu\text{m}$), as shown in Fig. 3(d). We found that the two near-perfect absorption peaks of the experimentally prepared metasurface absorber moved to $9.35 \mu\text{m}$ and $13.59 \mu\text{m}$, and the peak absorptions are 97.9% and 97%, respectively, where absorption (A) = 1 – transmittance (T) – reflectance (R). The average absorption is 90.36% in the infrared region of 8 to $14 \mu\text{m}$. However, the two near-perfect absorption peaks of the corresponding absorber in the simulation are located at $9.42 \mu\text{m}$ and $12.25 \mu\text{m}$, and the peak absorptions are 97.2% and 97.6%, respectively. The slight difference between the two absorption spectra may be caused by the material refractive index difference between experiment and simulation, and the imperfection of the structure of the prepared sample.

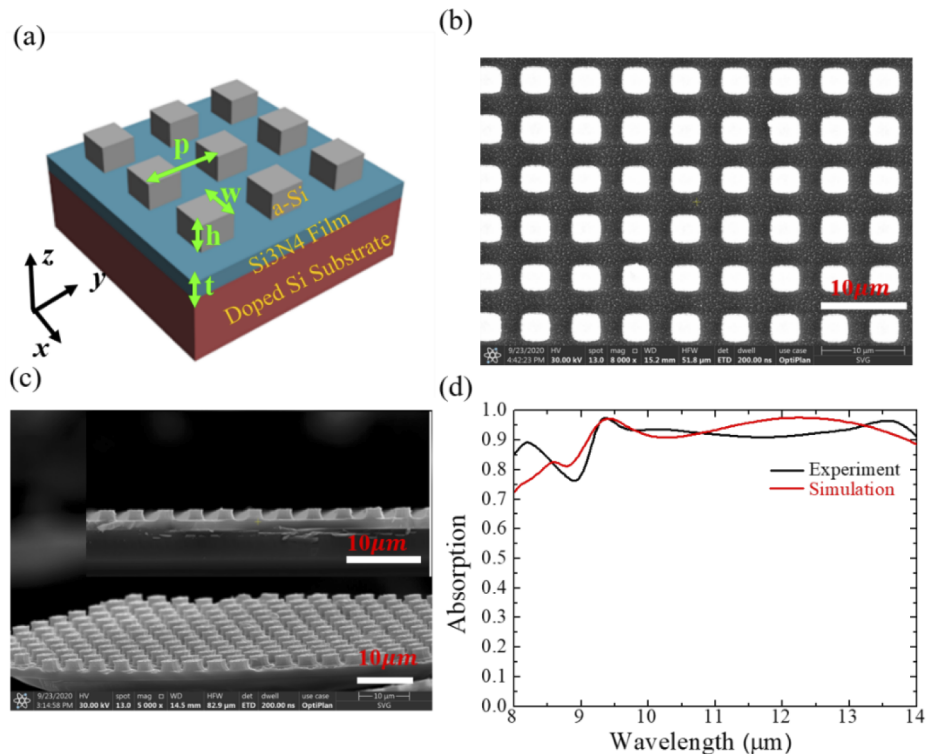


Fig. 3. (a) Schematic representation of the proposed all-metasurface absorber, consisting of Si resonator array, Si_3N_4 film, and Si substrate, with $h = 2.85 \mu\text{m}$, $w = 3.25 \mu\text{m}$, period $p = 6 \mu\text{m}$, $t = 2 \mu\text{m}$. (b) SEM image of an experimental sample (Scale bar: $10 \mu\text{m}$). (c) SEM image taken at an oblique angle of the experimental sample (Scale bar: $10 \mu\text{m}$). Inset is the cross-section SEM image of the experimental sample (Scale bar: $10 \mu\text{m}$). (d) Measured and simulated absorption spectra of the all-dielectric metasurface absorber.

As far as we know, for metasurfaces composed of periodic structures, the period plays an important role in the spectral response. Therefore, we numerically studied the influence of the period on the absorption spectrum of the metasurface absorber, as shown in Fig. 8(a). As the period changes, the absorption in the $8 \sim 10 \mu\text{m}$ region is decreasing, while the absorption in the $10 \sim 14 \mu\text{m}$ region is increasing. Therefore, in order to obtain the maximum average absorption in

the 8 ~ 14 μm region as much as possible, the period is fixed at 6 μm . To analyze the influence of the width and height of the resonator on the absorption spectrum of the all-dielectric metasurface, we also numerically investigated the absorption spectra of resonators with different width and height using the FDTD method in CST Microwave Studio. Figure 4(a) displays the effect of the resonator width on the absorption spectrum of the all-dielectric metasurface absorber. The perfect absorption peak at short wavelengths blue shifts as the resonator width decreases. This is because the absorption peak at the short wavelength is only caused by the resonance of the electric dipole, and the resonance frequency of the electric dipole is shifted as the width of the resonator changes [55,56]. Yet, the perfect absorption peak at the long wavelength appears only as a slight frequency shift with a large half-width. This is largely because the long-wavelength absorption peak is triggered by the coupling between the magnetic dipole resonance of the Si resonator at 11.89 μm and the TO phonon resonance of the Si_3N_4 at 12.2 μm , so that it is not very sensitive to changes in the size of the resonator [57]. We experimentally synthesized metasurface absorbers composed of three resonators with different widths. The width of the three resonators are 2.6 μm , 2.9 μm and 3.05 μm respectively. Figures 4(b), (c), (d) show their absorption spectra, and the insets are SEM images of their respective structures. Their absorption peaks at short wavelengths are 8.4 μm , 9.04 μm , and 9.35 μm , and at long wavelengths are 13.45 μm , 13.36 μm , and 13.59 μm , respectively, which confirm the inferences discussed above. The slight deviation

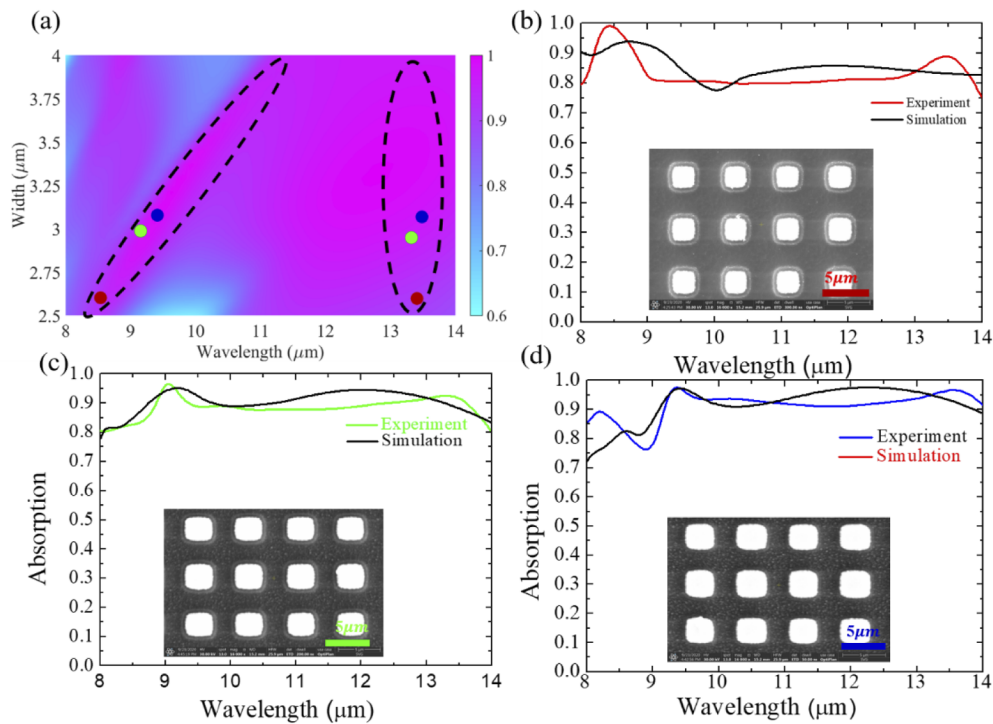


Fig. 4. (a) Simulated absorption of all-dielectric metasurface absorber as a function of wavelength and width of Si resonator. The two dashed boxes in the figure indicate the influence of the resonator width on the spectral positions of the short-wavelength and long-wavelength absorption peaks. The three points of red, green and blue correspond to the spectral positions of the absorption peaks of the synthesized three resonator widths. (b, c, d) The absorption curves of experimental samples and simulation results with different Si resonator widths, 2.6, 2.9, 3.05 μm , respectively. Inset is the SEM image of the experimental samples (Scale bar: 5, 5, 5 μm).

between the experimental results and the simulation results in Figs. 4(b, c, d) may come from two aspects. The surface roughness of the samples prepared in the experiment caused some light scattering. It also may be caused by the deviation between the refractive index of the experimental material and the value used in simulation.

The influence of the height of the resonator on the absorption spectrum is also discussed. The influence of the change in the height of the resonator on the absorption spectrum is similar to that of the change in the width, as shown in Fig. 8(b), but the influence is not so severe.

The angle-tolerant absorbance is critical for the metasurface absorber, as high absorbance in wide-angle is necessary in some applications. To investigate the angular response of absorption performance of the all-dielectric metasurface absorber, additional numerical simulations were implemented. Figures 5(a, b) display the numerically simulated absorbance of the metasurface absorber as a function of wavelength and incident angle for both transverse electric (TE, x-polarized, incident angle is in x-z plane) and transverse magnetic (TM, y-polarized, incident angle is in x-z plane) polarizations. Compared to the TM polarization oblique incidence, the absorption performance of the metasurface absorber reveals greater angular sensitivity to TE polarization incidence, which is primarily due to the fact that the electric field component interacting with the silicon resonator decreases with the increase in the angle of incidence. To approximate an unpolarized infrared absorption, Fig. 5(c) illustrates the arithmetic average of the numerically simulated absorbance of the metasurface absorber under TM and TE polarized excitations. These results indicate that the average absorption of the metasurface absorber for TE polarization, TM polarization, and unpolarization are 84.61%, 91.92%, and 88.27% at 40° angle of incidence. The calculated absorbance has confirmed the result that even under the condition of 40° oblique incidence, the absorber maintains high absorptivity.

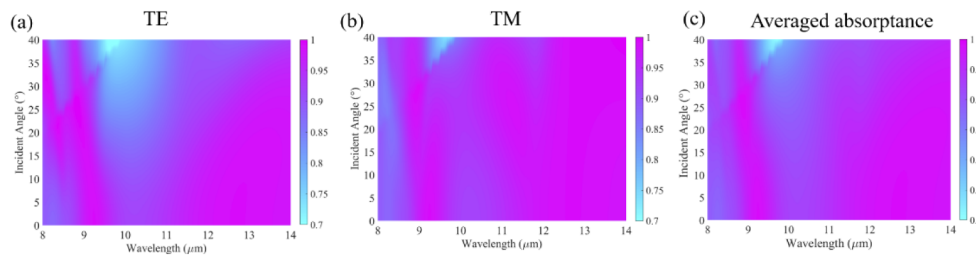


Fig. 5. (a, b) Simulated absorbance as a function of wavelength and incident angle under TM- and TE- polarized excitations. (c) Arithmetically averaged absorbance under TM- and TE- polarized excitations.

Microbolometer requires the imaging pixel to have higher spatially selective absorption characteristics, so that the thermal imaging has a higher contrast. To elucidate the practical application prospects of the designed all-dielectric metasurface absorber, we experimentally prepared a patterned metasurface, which exhibits spatially selective absorption property. Figure 6(a) displays the sample image of the patterned metasurface, printing the two letters “IR”. The sample size is 2 cm × 3 cm, contains more than 6.6 million resonators, and its processing only takes about 25 min by MLDWL. Thermal imaging of the patterned metasurface shows that the temperature at the resonator structure is 113 °C in Fig. 6(b), while the temperature at the flat surface is only 95.7 °C, displaying good spatially selective absorption (emission) property. Also, the designed metasurface absorber is composed of amorphous Si and Si₃N₄ materials, which are consistent with the materials used in currently available commercial microbolometers, and its preparation process is compatible with the CMOS processing technology. These advantages make it highly suitable for use in microbolometers. Here, we built a model to demonstrate that our proposed metasurface absorber can be integrated into a microbolometer. Considering the thermal time

constant to be proportional to the thermal mass of the absorption membrane of the microbolometer, we adjusted the structural parameters of the metasurface absorber to shorten the response time without significantly affecting the absorption performance. The optimized structural parameters are $h = 2 \mu\text{m}$, $w = 3 \mu\text{m}$, $p = 6 \mu\text{m}$, and $t = 1 \mu\text{m}$. The absorption spectrum of the metasurface absorber with the above structural parameters is presented in the Fig. 9(a). We used absorption as the heat source to simulate thermal radiation and heat transfer and chose amorphous silicon as the thermistor layer, as shown in Fig. 9(b). Figure 6(c) displays the steady-state temperature distribution of the entire device under an irradiation of 0.408 W/cm^2 infrared light power density. The temperature of the entire plane above the isolated thermal pillars reached 293.61 K , higher than room temperature of 293.15 K . At the same time, we also studied the transient response of the microbolometer integrated with the all-dielectric metasurface absorber. Figure 6(d) shows that after the input infrared radiation is irradiated for 5 ms , the temperature reaches a steady state. Also, after the input infrared radiation is turned off, the temperature drops to room temperature in 3 ms . From the above observation, it can be inferred that the temperature response and spatially selective absorption properties indicate that the designed metasurface absorber has the prospect of being applied to microbolometers.

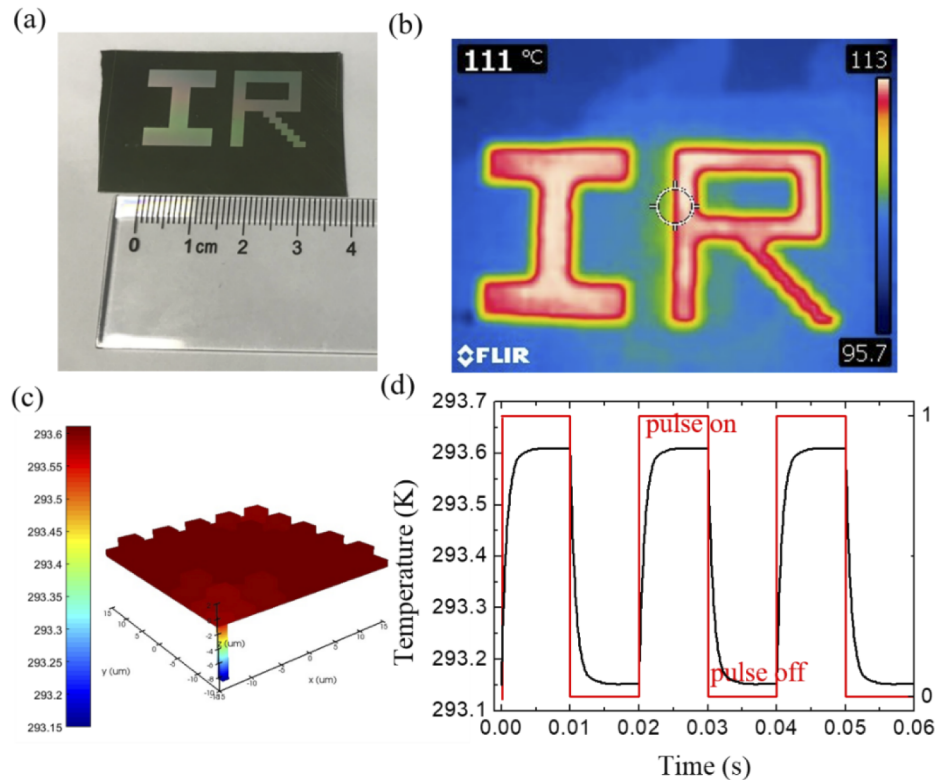


Fig. 6. (a) An image of the patterned spatially dispersive metasurface. (b) Thermal image of patterned spatially dispersive metasurface. (c) Steady-state temperature distribution of the microbolometer. The surrounding temperature is 293.15 K . (d) Transient temperature response of the microbolometer. The input pulse is 0 to 10 ms .

4. Conclusion

In summary, we have proposed and prepared an all-dielectric broadband metasurface absorber for the long-wave infrared spectral range. In design, we utilized square silicon resonators to excite multiple electric and magnetic dipole resonances to improve the absorption by the silicon nitride film, and used magnetic dipole resonance and TO phonon resonance coupling to produce an abnormally perfect absorption peak, which does not produce a shift in frequency as the size of the resonator changes. Numerical simulations prove that even when the incident angle reaches 40° , the metasurface absorber can still maintain an absorptivity above 88.27% in the $8 \sim 14 \mu\text{m}$ spectral range. Besides, the designed metasurface absorber has the advantages of simple structure and easy preparation. The fabricated large-area patterned metasurface absorber using maskless laser direct writing technology displays spatially selective absorption properties and its potential for integration with microbolometers.

Appendix

1. Simulated power loss density distribution

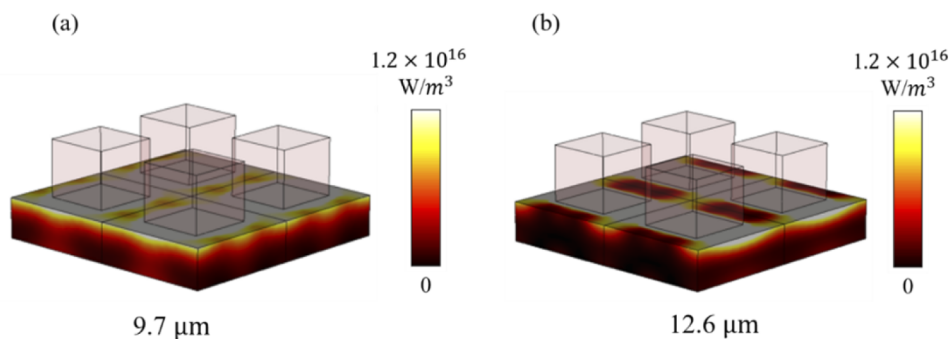


Fig. 7. (a,b) Simulated power loss density distributions at resonance peaks of 9.7 and $12.6 \mu\text{m}$, respectively.

2. The influence of geometric parameters on absorption spectrum

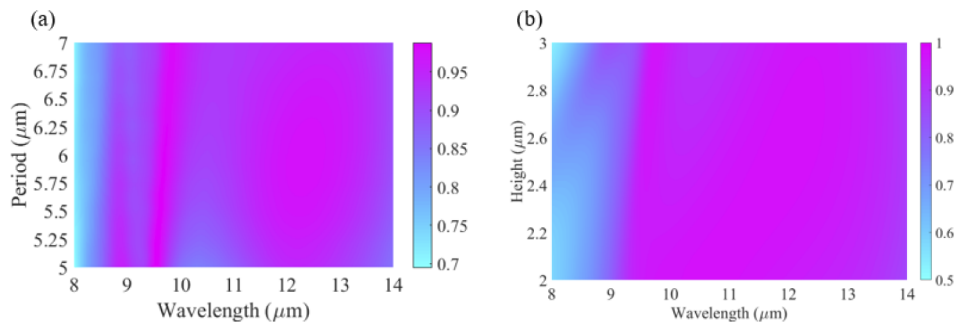


Fig. 8. (a) The influence of period on absorption spectrum. (b) The influence of Si resonator height on the absorption spectrum.

3. The absorption spectrum and heat source of the designed microbolometer

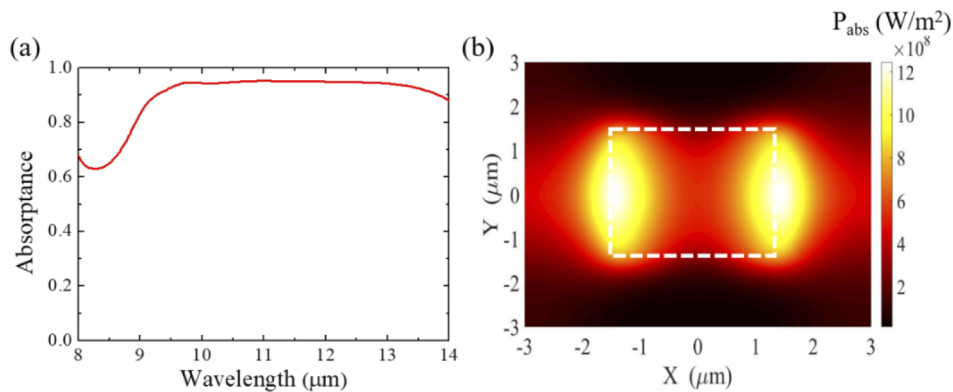


Fig. 9. (a) The absorption spectrum of the metasurface absorber with the structural parameters $h = 2 \mu\text{m}$, $w = 3 \mu\text{m}$, $p = 6 \mu\text{m}$, and $t = 1 \mu\text{m}$. (b) The heat source to simulate thermal radiation and heat transfer.

Funding. National Natural Science Foundation of China (11690033, 61974100); National Key Research and Development Program of China (2017YFA0205700, 2017YFA0303702); Natural Science Research of Jiangsu Higher Education Institutions of China (20KJA480002); Natural Science Foundation of Jiangsu Province (BK20181166).

Disclosures. The authors declare no conflicts of interest.

Data availability. Data underlying the results presented in this paper are not publicly available at this time but may be obtained from the authors upon reasonable request.

References

1. M. W. Knight, H. Sobhani, P. Nordlander, and N. J. Halas, "Photodetection with Active Optical Antennas," *Science* **332**(6030), 702–704 (2011).
2. X. Gan, R.-J. Shiue, Y. Gao, I. Meric, T. F. Heinz, K. Shepard, J. Hone, S. Assefa, and D. Englund, "Chip-integrated ultrafast graphene photodetector with high responsivity," *Nat. Photonics* **7**(11), 883–887 (2013).
3. Y. Zhai, Y. Ma, S. N. David, D. Zhao, R. Lou, G. Tan, R. Yang, and X. Yin, "Scalable-manufactured randomized glass-polymer hybrid metamaterial for daytime radiative cooling," *Science* **355**(6329), 1062–1066 (2017).
4. M. M. Hossain, B. Jia, and M. Gu, "A Metamaterial Emitter for Highly Efficient Radiative Cooling," *Adv. Opt. Mater.* **3**(8), 1047–1051 (2015).
5. C. Zou, G. Ren, M. M. Hossain, S. Nirantar, W. Withayachumnankul, T. Ahmed, M. Bhaskaran, S. Sriram, M. Gu, and C. Fumeaux, "Metal-Loaded Dielectric Resonator Metasurfaces for Radiative Cooling," *Adv. Opt. Mater.* **5**(20), 1700460 (2017).
6. X. Pan, H. Xu, Y. Gao, Y. Zhang, L. Sun, D. Li, Z. Wen, S. Li, W. Yu, Z. Huang, J. Wang, B. Zhang, Y. Sun, J. Sun, X. Meng, X. Chen, B. Dagens, J. Hao, Y. Shen, N. Dai, and J. Chu, "Spatial and Frequency Selective Plasmonic Metasurface for Long Wavelength Infrared Spectral Region," *Adv. Opt. Mater.* **6**(20), 1800337 (2018).
7. X. Liu, T. Starr, A. F. Starr, and W. J. Padilla, "Infrared Spatial and Frequency Selective Metamaterial with Near-Unity Absorbance," *Phys. Rev. Lett.* **104**(20), 207403 (2010).
8. J. Suen, K. Fan, J. Montoya, C. Bingham, V. Stenger, S. Sriram, and W. Padilla, "Multifunctional metamaterial pyroelectric infrared detectors," *Optica* **4**(2), 276–279 (2017).
9. N. Liu, M. Mesch, T. Weiss, M. Hentschel, and H. Giessen, "Infrared Perfect Absorber and Its Application As Plasmonic Sensor," *Nano Lett.* **10**(7), 2342–2348 (2010).
10. K. Chen, R. Adato, and H. Altug, "Dual-Band Perfect Absorber for Multispectral Plasmon-Enhanced Infrared Spectroscopy," *ACS Nano* **6**(9), 7998–8006 (2012).
11. C. Wu, B. Neuner Iii, J. John, A. Milder, B. Zollars, S. Savoy, and G. Shvets, "Metamaterial-based integrated plasmonic absorber/emitter for solar thermo-photovoltaic systems," *J. Opt.* **14**(2), 024005 (2012).
12. L. P. Wang and Z. M. Zhang, "Wavelength-selective and diffuse emitter enhanced by magnetic polaritons for thermophotovoltaics," *Appl. Phys. Lett.* **100**(6), 063902 (2012).
13. E. Rephaeli and S. Fan, "Absorber and emitter for solar thermo-photovoltaic systems to achieve efficiency exceeding the Shockley-Queisser limit," *Opt. Express* **17**(17), 15145–15159 (2009).
14. S. Ogawa, D. Fujisawa, H. Hata, M. Uetsuki, K. Misaki, and M. Kimata, "Mushroom plasmonic metamaterial infrared absorbers," *Appl. Phys. Lett.* **106**(4), 041105 (2015).

15. J. Jung, J. Lee, D. Choi, J. Choi, J. Jeong, E. Lee, and D. P. Neikirk, "Wavelength-Selective Infrared Metasurface Absorber for Multispectral Thermal Detection," *IEEE Photonics J.* **7**(6), 1–10 (2015).
16. A. Howes, J. R. Nolen, J. D. Caldwell, and J. Valentine, "Near-Unity and Narrowband Thermal Emissivity in Balanced Dielectric Metasurfaces," *Adv. Opt. Mater.* **8**(4), 1901470 (2020).
17. W. Ma, D. Jia, Y. Wen, X. Yu, Y. Feng, and Y. Zhao, "Diode-based microbolometer with performance enhanced by broadband metamaterial absorber," *Opt. Lett.* **41**(13), 2974–2977 (2016).
18. A. Safaei, S. Modak, J. Lee, S. Chandra, D. Franklin, A. Vázquez-Guardado, and D. Chanda, "Multi-spectral frequency selective mid-infrared microbolometers," *Opt. Express* **26**(25), 32931–32940 (2018).
19. K. Du, Q. Li, W. Zhang, Y. Yang, and M. Qiu, "Wavelength and Thermal Distribution Selectable Microbolometers Based on Metamaterial Absorbers," *IEEE Photonics J.* **7**(3), 1–8 (2015).
20. M. Mahjour-Samani, Y. S. Zhou, X. N. He, W. Xiong, P. Hilger, and Y. F. Lu, "Plasmonic-enhanced carbon nanotube infrared bolometers," *Nanotechnology* **24**(3), 035502 (2013).
21. S. Shrestha, Y. Wang, A. C. Overvig, M. Lu, A. Stein, L. D. Negro, and N. Yu, "Indium Tin Oxide Broadband Metasurface Absorber," *ACS Photonics* **5**(9), 3526–3533 (2018).
22. N. I. Landy, S. Sajuyigbe, J. J. Mock, D. R. Smith, and W. J. Padilla, "Perfect Metamaterial Absorber," *Phys. Rev. Lett.* **100**(20), 207402 (2008).
23. C. M. Watts, X. Liu, and W. J. Padilla, "Metamaterial Electromagnetic Wave Absorbers," *Adv. Mater.* **24**(23), OP98–OP120 (2012).
24. X. Liu, T. Tyler, T. Starr, A. F. Starr, N. M. Jokerst, and W. J. Padilla, "Taming the Blackbody with Infrared Metamaterials as Selective Thermal Emitters," *Phys. Rev. Lett.* **107**(4), 045901 (2011).
25. X. Zhang, H. Liu, Z. G. Zhang, Q. Wang, and S. N. Zhu, "Controlling thermal emission of phonon by magnetic metasurfaces," *Sci. Rep.* **7**(1), 41858 (2017).
26. X. Zhang, Z. G. Zhang, Q. Wang, S. N. Zhu, and H. Liu, "Controlling Thermal Emission by Parity-Symmetric Fano Resonance of Optical Absorbers in Metasurfaces," *ACS Photonics* **6**(11), 2671–2676 (2019).
27. J. Tao, Z. Liang, G. Zeng, D. Meng, D. R. Smith, Q. H. Liu, Q. Yang, M. Zhang, W. Pang, and J. Liang, "Dual functionality metamaterial enables ultra-compact, highly sensitive uncooled infrared sensor," *Nanophotonics* **10**(4), 1337–1346 (2021).
28. J. A. Bossard, L. Lin, S. Yun, L. Liu, D. H. Werner, and T. S. Mayer, "Near-Ideal Optical Metamaterial Absorbers with Super-Octave Bandwidth," *ACS Nano* **8**(2), 1517–1524 (2014).
29. Y. Zhou, Z. Qin, Z. Liang, D. Meng, H. Xu, D. R. Smith, and Y. Liu, "Ultra-broadband metamaterial absorbers from long to very long infrared regime," *Light: Sci. Appl.* **10**(1), 138 (2021).
30. Y. Zhou, Z. Liang, Z. Qin, X. Shi, and X. Wang, "Broadband long wavelength infrared metamaterial absorbers," *Results Phys.* **19**, 103566 (2020).
31. Z. Qin, D. Meng, F. Yang, X. Shi, Z. Liang, H. Xu, D. R. Smith, and Y. Liu, "Broadband long-wave infrared metamaterial absorber based on single-sized cut-wire resonators," *Opt. Express* **29**(13), 20275–20285 (2021).
32. C. Cheng, M. Abbas, C. Chiu, K. Lai, M. Shih, and Y. Chang, "Wide-angle polarization independent infrared broadband absorbers based on metallic multi-sized disk arrays," *Opt. Express* **20**(9), 10376–10381 (2012).
33. M. Ghaderi, E. Shahmarvandi, and R. Wölfenbuttel, "CMOS-compatible mid-IR metamaterial absorbers for out-of-band suppression in optical MEMS," *Opt. Mater. Express* **8**(7), 1696–1707 (2018).
34. W. Guo, Y. Liu, and T. Han, "Ultra-broadband infrared metasurface absorber," *Opt. Express* **24**(18), 20586–20592 (2016).
35. Y. Cui, K. H. Fung, J. Xu, H. Ma, Y. Jin, S. He, and N. X. Fang, "Ultrabroadband Light Absorption by a Sawtooth Anisotropic Metamaterial Slab," *Nano Lett.* **12**(3), 1443–1447 (2012).
36. Q. Liang, T. Wang, Z. Lu, Q. Sun, Y. Fu, and W. Yu, "Metamaterial-Based Two Dimensional Plasmonic Subwavelength Structures Offer the Broadest Waveband Light Harvesting," *Adv. Opt. Mater.* **1**(1), 43–49 (2013).
37. Y. Tang, D. Meng, Z. Liang, Z. Qin, and J. Lai, "An Infrared Metamaterial Broadband Absorber Based on a Simple Titanium Disk with High Absorption and a Tunable Spectral Absorption Band," *Ann. Phys.* **532**(9), 2000145 (2020).
38. D. Ji, H. Song, X. Zeng, H. Hu, K. Liu, N. Zhang, and Q. Gan, "Broadband absorption engineering of hyperbolic metafilm patterns," *Sci. Rep.* **4**(1), 4498 (2015).
39. J. Zhou, A. F. Kaplan, L. Chen, and L. J. Guo, "Experiment and Theory of the Broadband Absorption by a Tapered Hyperbolic Metamaterial Array," *ACS Photonics* **1**(7), 618–624 (2014).
40. K. Gorgulu, A. Gok, M. Yilmaz, K. Topalli, N. Bıyıklı, and A. K. Okyay, "All-silicon ultra-broadband infrared light absorbers," *Sci. Rep.* **6**(1), 38589 (2016).
41. S. Wang, Y. Wang, S. Zhang, and W. Zheng, "Mid-infrared broadband absorber of full semiconductor epi-layers," *Phys. Lett. A* **381**(16), 1439–1444 (2017).
42. Y. Zhou, Z. Liang, Z. Qin, E. Hou, X. Shi, Y. Zhang, Y. Xiong, Y. Tang, Y. Fan, F. Yang, J. Liang, C. Chen, and J. Lai, "Small-sized long wavelength infrared absorber with perfect ultra-broadband absorptivity," *Opt. Express* **28**(2), 1279–1290 (2020).
43. W. Yu, Y. Lu, X. Chen, H. Xu, J. Shao, X. Chen, Y. Sun, J. Hao, and N. Dai, "Large-Area, Broadband, Wide-Angle Plasmonic Metasurface Absorber for Midwavelength Infrared Atmospheric Transparency Window," *Adv. Opt. Mater.* **7**(20), 1900841 (2019).

44. F. Bezares, J. Long, O. Glembocki, J. Guo, R. Rendell, R. Kasica, L. Shirey, J. Owrutsky, and J. Caldwell, "Mie resonance-enhanced light absorption in periodic silicon nanopillar arrays," *Opt. Express* **21**(23), 27587–27601 (2013).
45. I. Staude, A. E. Miroshnichenko, M. Decker, N. T. Fofang, S. Liu, E. Gonzales, J. Dominguez, T. S. Luk, D. N. Neshev, I. Brener, and Y. Kivshar, "Tailoring Directional Scattering through Magnetic and Electric Resonances in Subwavelength Silicon Nanodisks," *ACS Nano* **7**(9), 7824–7832 (2013).
46. L. R. de Kronig, "On the Theory of Dispersion of X-Rays," *J. Opt. Soc. Am.* **12**(6), 547–557 (1926).
47. B. Slovick, Z. G. Yu, M. Berding, and S. Krishnamurthy, "Perfect dielectric-metamaterial reflector," *Phys. Rev. B* **88**(16), 165116 (2013).
48. Y. Huang, H. Xu, Y. Lu, and Y. Chen, "All-dielectric metasurface for achieving perfect reflection at visible wavelengths," *J. Phys. Chem. C* **122**(5), 2990–2996 (2018).
49. Z. Ma, S. M. Hanham, P. Albella, B. Ng, H. T. Lu, Y. Gong, S. A. Maier, and M. Hong, "Terahertz all-dielectric magnetic mirror metasurfaces," *ACS Photonics* **3**(6), 1010–1018 (2016).
50. P. Moitra, B. A. Slovick, W. Li, I. I. Kravchenko, D. P. Briggs, S. Krishnamurthy, and J. Valentine, "Large-scale all-dielectric metamaterial perfect reflectors," *ACS Photonics* **2**(6), 692–698 (2015).
51. D. Chandler-Horowitz and P. M. Amirtharaj, "High-accuracy, midinfrared ($450\text{cm}^{-1} \leq \omega \leq 4000\text{cm}^{-1}$) refractive index values of silicon," *J. Appl. Phys.* **97**(12), 123526 (2005).
52. J. Kischkat, S. Peters, B. Gruska, M. Semtsiv, M. Chashnikova, M. Klinkmüller, O. Fedosenko, S. Machulik, A. Aleksandrova, G. Monastyrskyi, Y. Flores, and W. T. Masselink, "Mid-infrared optical properties of thin films of aluminum oxide, titanium dioxide, silicon dioxide, aluminum nitride, and silicon nitride," *Appl. Opt.* **51**(28), 6789–6798 (2012).
53. K. Üstün and G. Turhan-Sayan, "Wideband long wave infrared metamaterial absorbers based on silicon nitride," *J. Appl. Phys.* **120**(20), 203101 (2016).
54. J. Tian, H. Luo, Q. Li, X. Pei, K. Du, and M. Qiu, "Near-Infrared Super-Absorbing All-Dielectric Metasurface Based on Single-Layer Germanium Nanostructures," *Laser Photonics Rev.* **12**(9), 1800076 (2018).
55. P. Moitra, B. A. Slovick, Z. Gang Yu, S. Krishnamurthy, and J. Valentine, "Experimental demonstration of a broadband all-dielectric metamaterial perfect reflector," *Appl. Phys. Lett.* **104**(17), 171102 (2014).
56. C. Chen, Z.-Y. Wang, Z.-G. Zheng, Y. Liu, W. Huang, and L. Chen, "Large-area, low-cost near-infrared meta-surface reflector based on a pixelated two-dimensional silicon disk array," *Opt. Express* **28**(25), 38355–38365 (2020).
57. X. Zhao, C. Chen, A. Li, G. Duan, and X. Zhang, "Implementing infrared metamaterial perfect absorbers using dispersive dielectric spacers," *Opt. Express* **27**(2), 1727–1739 (2019).